Short timescale behavior of colliding heavy nuclei at intermediate energies

S. Hudan and R. T. de Souza
Department of Chemistry and Indiana University Cyclotron Facility Indiana University, Bloomington, Indiana 47405, USA

A. Ono
Department of Physics, Tohoku University, Sendai 980-8578, Japan

(Received 26 September 2005; published 4 May 2006)

Noncentral collisions of ^{114}Cd projectiles with ^{92}Mo target nuclei at $E/A = 50$ MeV are explored with an antisymmetrized molecular dynamics model. These collisions are found to be essentially binary in character with formation of an excited projectile-like fragment (PLF*) and targetlike fragment (TLF*). The average excitation energy deduced for the PLF* and TLF* saturates for midcentral collisions, $3.5 \leqslant b \leqslant 6$ fm, with its magnitude depending on the cluster recognition time. For short cluster recognition times ($t = 150$ fm/c), an average excitation energy as high as $\approx$6 MeV is determined, indicating a short statistical lifetime for the fragments produced. Evidence for such a rapid deexcitation is observed in the present calculations.

DOI: 10.1103/PhysRevC.73.054602 PACS number(s): 25.70.Mn, 24.10.Lx, 27.70.Pq

I. INTRODUCTION

Collision of two heavy ions at intermediate energies can result in the production of a multiparticle final state [1–3]. These multiparticle final states have been experimentally characterized by a wide variety of signals, including fragment multiplicity [1,2], size distributions [4,5], emission timescales [6–9], scaling behavior [10–12], and the excitation energy attained [13]. For large fragment multiplicity, within a thermodynamic approach, such multifragment states have been interpreted as a transition of the finite nuclear system from a liquid to a gaseous phase [14–17]. Recent work has investigated the robustness of this conclusion by examining the influence of the surface, through the density dependence of the entropy, on the stability of the nuclear droplet against fragmentation [18,19]. All these approaches, however, focus on the thermodynamic stability of the system. In reality, the decaying system is formed by the collision dynamics that may not equilibrate all degrees of freedom equally [20,21]. To understand both the formation and decay of excited nuclear systems involved in the collision process, microscopic approaches have also been followed [22–33]. Previous studies have often been restricted to classical molecular dynamics simulations [22,27,29–31], in some cases neglecting the Coulomb interaction [31] and in other cases confining the system artificially to a box [22,27]. Such restrictions complicate the direct comparison with experimental data.

A further conceptual problem is the two-stage approach typically utilized by such microscopic models. In the first phase, a dynamical model is used to describe the collision dynamics. Clusters produced in this phase are subsequently deexcited by a statistical model. Such a two-stage approach typically views the statistical decay stage as relatively decoupled from the dynamical stage that preceded it. In the present work we examine the validity of such a decoupled hybrid approach. Specifically, we utilize a microscopic model, the antisymmetrized molecular dynamics (AMD) model, to investigate how the collision proceeds on short timescales and how the reaction characteristics evolve with impact parameter. In addition, we examine whether initial correlations, existing at short times, survive the decay stage and how they are manifested in final distributions.

II. DESCRIPTION OF THE AMD MODEL

To describe the dynamical stage of intermediate energy heavy-ion collisions, we utilize the AMD model [34–37]. For the present work, we use the same version of AMD as Ref. [36], which has been used to describe the multifragmentation reaction of the central Xe+Sn collisions at 50 MeV/nucleon.

The description of the dynamics of fragmentation is, in principle, a very complicated quantum many-body problem. In the exact solution of the many-body time-dependent Schrödinger equation, the intermediate and final states should be very complicated states containing a huge number of reaction channels corresponding to different fragmentation configurations. The AMD model respects the existence of channels, whereas it neglects some of the interference among them. Namely the total many-body wave function $|\Psi(t)\rangle$ is approximated by

$$|\Psi(t)\rangle\langle\Psi(t)| \approx \int \frac{|\Phi(Z)\rangle\langle\Phi(Z)|}{\langle\Phi(Z)|\Phi(Z)\rangle} w(Z,t) dZ, \qquad (1)$$

where each channel wave function $|\Phi(Z)\rangle$ is parametrized by a set of parameters Z and $w(Z,t)$ is the time-dependent probability of each channel.

In AMD, we choose the Slater determinant of Gaussian wave packets as the channel wave function

$$\langle \mathbf{r}_1 \ldots \mathbf{r}_A | \Phi(Z)\rangle \propto \det_{ij}[\exp\{-\nu(\mathbf{r}_i - \mathbf{Z}_j/\sqrt{\nu})2\}\chi_{\alpha_j}(i)], \quad (2)$$

where χ_{α_i} are the spin-isospin states with $\alpha_i = p\uparrow, p\downarrow, n\uparrow$, or $n\downarrow$. Thus, the many-body state $|\Phi(Z)\rangle$ is parametrized by a set of complex variables $Z \equiv \{\mathbf{Z}_i\}_{i=1,\ldots,A}$, where A is the number of nucleons in the system. The width parameter, $\nu = 0.16$ fm^{-2}, is treated as a constant parameter common to all

the wave packets. If we ignore the antisymmetrization effect, the real part of $\mathbf{Z}_i$ corresponds to the position centroid and the imaginary part corresponds to the momentum centroid. This choice of channel wave functions is suitable for fragmentation reactions, where each single-particle wave function should be localized within a fragment.

Instead of directly considering the probability $w(Z, t)$ in Eq. (1), we solve a stochastic equation of motion for the wave-packet centroids Z, which may be symbolically written as

$$\frac{d}{dt}\mathbf{Z}_i = \{\mathbf{Z}_i, \mathcal{H}\}_{\rm PB} + (\text{NN coll}) + \Delta\mathbf{Z}_i(t) + \mu\,(\mathbf{Z}_i, \mathcal{H}'). \quad (3)$$

The first term $\{\mathbf{Z}_i, \mathcal{H}\}_{\rm PB}$ is the deterministic term derived from the time-dependent variational principle with an assumed effective interaction. The Gogny interaction [38] is used in the present work. The second term represents the effect of the stochastic two-nucleon collision process, where a parametrization of the energy-dependent in-medium cross section is adopted. The two-nucleon collision cross section used is the same as in Ref. [36], namely

$$\sigma(E, \rho) = \min\left[\sigma_{\rm LM}(E, \rho), \frac{100\ \text{mb}}{1 + E/(200\text{MeV})}\right], \quad (4)$$

The collisions are performed with the "physical nucleon coordinates" that take account of the antisymmetrization effects, and then the Pauli blocking in the final state is automatically introduced [34,35]. The third term $\Delta\mathbf{Z}_i(t)$ is a stochastic fluctuation term that has been introduced to respect the change of the width and shape of the single particle distribution [36,39,40]. In other words, the combination $\{\mathbf{Z}_i, \mathcal{H}\}_{\rm PB} + \Delta\mathbf{Z}_i(t)$ approximately reproduces the prediction by mean-field theories (for a short time period) for the ensemble-averaged single-particle distribution, whereas each nucleon is localized in phase space for each channel. The term $\Delta\mathbf{Z}_i(t)$ is calculated practically by solving the Vlasov equation (for a short time period) with the same effective interaction as for the term $\{\mathbf{Z}_i, \mathcal{H}\}_{\rm PB}$. In the present version of AMD [36], the property of the fluctuation $\Delta\mathbf{Z}_i(t)$ is chosen in such a way that the coherent single-particle motion in the mean field is respected for some time interval until the nucleon collides another nucleon. The last term $\mu\,(\mathbf{Z}_i, \mathcal{H}')$ is a dissipation term related to the fluctuation term $\Delta\mathbf{Z}_i(t)$. The dissipation term is necessary to restore the conservation of energy that is violated by the fluctuation term. The coefficient μ is given by the condition of energy conservation. However, the form of this term is somehow arbitrary. We shift the variables Z to the direction of the gradient of the energy expectation value $\mathcal{H}$ under the constraints of conserved quantities (the center-of-mass variables and the total angular momentum) and global one-body quantities (monopole and quadrupole moments in coordinate and momentum spaces). A complete formulation of AMD can be found in Refs. [36,37].

At regular intervals, the positions and momenta of all nucleons in the system were recorded. At a selected time (typically 300 fm/c), which we designate the cluster recognition time, the nucleon distributions are subjected to a cluster recognition algorithm based on the distance between nucleons. The excitation energy of a cluster is based on the momentum of all constituents of the cluster, in its center-of-mass, relative to its ground-state binding energy. The nucleons and clusters that result from cluster recognition are subsequently propagated along Coulomb trajectories and allowed to statistically decay. The statistical decay of relatively small primary fragments ($Z < 20$) is calculated by using the code [41] based on the sequential binary decay model by Pühlhofer [42]. The code employed in the present work also takes account of the emission of composite particles not only in their ground states but also in their excited states with the excitation energy $E^* \leqslant 40$ MeV. The experimental information is incorporated for known levels of $A \lesssim 28$ nuclei, whereas the Fermi-gas level density is assumed otherwise. For the statistical decay of large primary fragments ($Z \geqslant 20$), the decay code GEMINI [43] is employed. In considering the decay of the fragments, both the excitation energy and decay probabilities are calculated for spherical fragments independent of the true shape of the fragments induced by the reaction dynamics. Introduction of a deformation dependence of the nuclear level density, and in particular the treatment of the continuum, results in a significant modification of the emission rate for fragments that are weakly bound or at high excitation [44]. In the present work, the effect of n-p asymmetry, excitation energy, and deformation on the nuclear level density are not considered in the decay.

The system we have chosen to study is ^{114}Cd+^{92}Mo at $E/A = 50$ MeV, which can be considered representative of symmetric heavy-ion collisions in this energy domain. We sampled all impact parameters, b, in the interval $0 \leqslant b \leqslant b_{\rm max}$ with a triangular distribution. The maximum impact parameter $b_{\rm max}$ had a value of 12 fm. The touching sphere configuration distance, given by $R = 1.2^*(A_P^{1/3} + A_T^{1/3})$, is equal to 11.2 fm. The projectile and target were therefore placed at an initial distance of 13 fm for $b \geqslant 6.5$ fm and 9.8 fm for b <6.5 fm. For a given collision, the fate of the colliding system was followed until 300 fm/c. The identity and momenta of the reaction products are recorded for subsequent analysis. These events are then subjected to the statistical decay code. To examine the predictions of this model in a statistically significant manner, we have amassed ≈25,000 collisions. The calculations were performed on a 646-CPU parallel processor system of which each CPU was either a PowerPC or Power3+. A single collision for this reaction required 12 to 24 CPU-hours depending on the impact parameter.

III. GENERAL REACTION CHARACTERISTICS

Depicted in Fig. 1 is the density distribution of nucleons in R space as a function of time for a midperipheral ($b =$ 7.79 fm) and midcentral ($b = 5.15$) collision. The initial moment in time ($t = 0$) is taken as the near touching configuration of the projectile-target system previously described, with the projectile approaching the target nucleus from the negative z direction. As the dinuclear system rotates, the initial dumbbell shape of the two touching nuclei shown in the top panel evolves. Although in contact, the two nuclei exchange mass, charge, and energy, governed by nucleon-nucleon scattering within the mean field.

For the presented event with $b = 7.79$ fm, one observes that two large nuclei emerge from the collision at

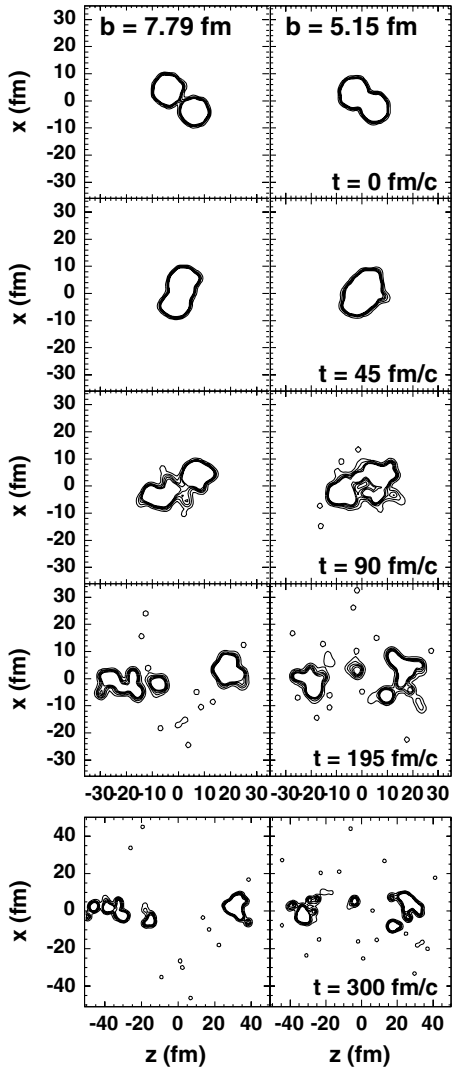

FIG. 1. Contour diagram depicting the nucleon density distribution in spatial coordinates as a function of time for the reaction ^{114}Cd+^{92}Mo at $E/A = 50$ MeV. The positive z direction corresponds to the direction of the projectile. The columns correspond to different impact parameters, $b = 7.79$ fm (left) and $b = 5.15$ fm (right).

$t = 90$ fm/c revealing the intrinsically binary nature of the collision. In this case, at longer times the elongation of the targetlike fragment (left) leads to its breakup into multiple intermediate size nuclei. In the case of the midcentral collision with $b = 5.15$ fm, however, the situation is more difficult to discern. At $t = 90$ fm/c, it is unclear whether the system is disassembling into two or three large pieces. What is apparent is that as the two nuclei separate from each other, one observes that the density distributions reflect the nuclear interaction between the projectile and target nuclei through the formation of transiently deformed nuclei. These nonspherical geometries persist up to 300 fm/c for different cluster sizes. Previous study of a confined system using classical molecular dynamics calculations also showed that clusters exhibit fractal shapes [30]. In this work by following the evolution of a self-bound cluster, it was observed that it relaxes its shape and becomes spherical. The highly deformed shapes of the transient clusters and their relaxation are features also present in the AMD calculations, namely they do not arise simply from the classical or confined nature of the previous work. For both events presented in Fig. 1 clusters seem to emerge on a relatively fast timescale, $t \approx 90$ fm/c. This early production of clusters indicates that the time scale of the shape/density fluctuations responsible for cluster formation operate on this time scale. It should be noted that a considerable fraction, *though not all*, of this early stage cluster emission is located between the two large fragments that emerge from the collision. Classical molecular dynamics calculations, where the Coulomb interaction is considered, also show that dynamical induced shape instabilities can lead to a significant emission of clusters at velocities intermediate between those of the two reaction partners [29]. The evolution of the density distributions presented in Fig. 1 can also be viewed from the context of semiclassical colliding liquid drops. Formation of the transiently extended nuclear system by the collision dynamics involves the generation of a considerable amount of "surface" nuclear material as compared to "bulk" nuclear material. In comparison to the original system comprised of the projectile and target nuclei, the multifragment final state with multiple clusters requires the formation of a significant amount of surface – an energetically unfavorable change. Thus, once the surface-to-volume ratio has been increased by the collision dynamics, the energy cost of the system reorganizing to the multifragment final state is considerably reduced.

We examine the characteristics of the system immediately following this dynamical stage of the collision. The products of the reaction at this stage are designated the "primary" products that statistically deexcite to form the final reaction products, which we refer to as the "secondary" products. For a large ensemble of events we examine the evolution of both primary and secondary distributions with impact parameter and cluster recognition time.

An overview of the collisions studied is presented in Fig. 2, where the correlation between the atomic number and parallel velocity (in the center-of-mass frame) of particles at $t = 300$ fm/c is examined. For the most peripheral collisions ($8.5 < b \leqslant 10$ fm) two peaks located at $Z \approx 47$ and ≈ 39 are clearly evident. These peaks correspond to the excited projectile-like (PLF*) and targetlike (TLF*) nuclei, respectively, and are relatively narrow distributions in velocity centered at $V_{\parallel} = 3.8$ and -4.7 cm/ns. Also evident is copious production of neutrons ($Z = 0$), hydrogen, and helium nuclei. Smaller in yield, are clusters with $Z \geqslant 3$ and atomic number less than that of the PLF* and TLF*. This pattern, dominated by the survival of the PLF* and TLF* for a peripheral collision, reflects a primarily binary nature. For midperipheral and midcentral collisions, a similar pattern is observed, indicating that in this impact parameter range as well a PLF* and TLF* survive the dynamical phase, hence these impact parameters are also essentially binary in character. With increasing centrality $\langle V_{\mathrm{PLF}^*} \rangle$ decreases and $\langle V_{\mathrm{TLF}^*} \rangle$ increases reflecting an increase in the velocity damping. At the same time, the width of the PLF* and TLF* velocity distributions increases indicating the growth of fluctuations. In addition, with increasing centrality the average atomic number of the PLF* and TLF* decreases, whereas the yield of clusters with $3 \leqslant Z \leqslant 15$ increases. For

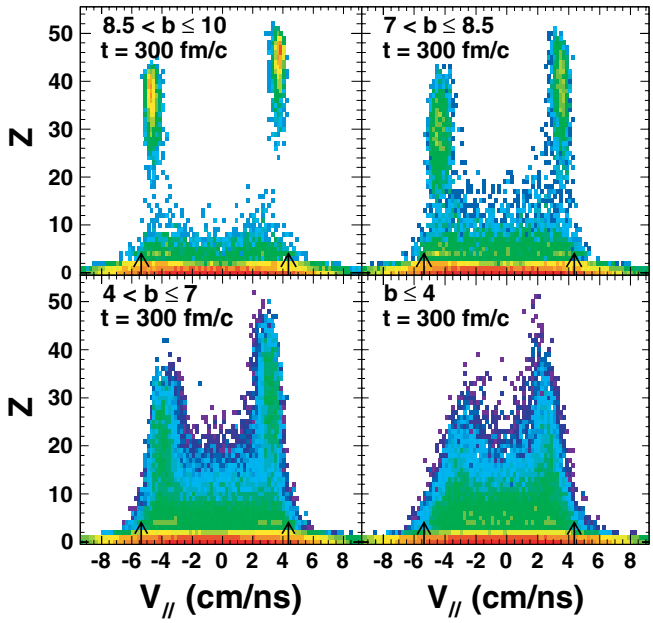

FIG. 2. (Color online) Two dimensional diagram of the correlation between the atomic number and parallel velocity of particles at $t = 300$ fm/c for different impact parameters. The arrows correspond to the projectile and target velocities. The color scale indicates the yield on a logarithmic scale.

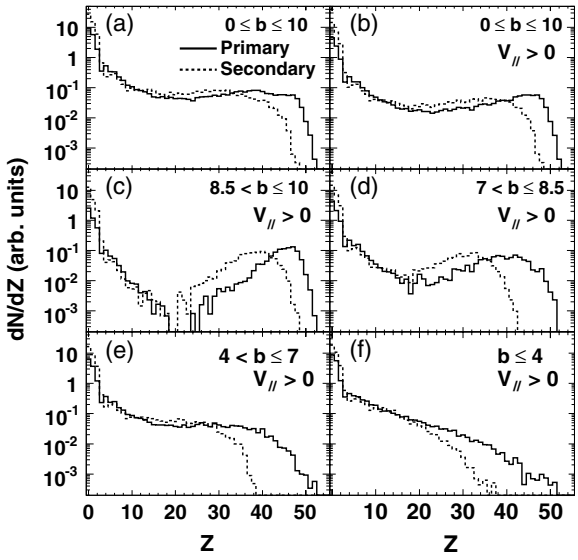

FIG. 3. Dependence of the primary (solid) and secondary (dashed) Z distributions on impact parameter. The differential yield dN/dZ has been normalized by the total number of events for each impact parameter interval.

simplicity, we designate the highest Z cluster with a velocity larger (smaller) than the center-of-mass velocity as the PLF* (TLF*). For $b \leqslant 4$ fm the decrease in the average Z of the PLF* combined with the width of the distribution leads to an operational definition of intermediate mass fragment, namely IMF: $3 \leqslant Z \leqslant 10$. Particles with $Z \leqslant 10$ manifest broad velocity distributions for the most central collisions. Examination of the most peripheral collisions reveals a clear pattern of how the velocity distribution evolves with the atomic number (Z) of the fragment. Neutrons and hydrogen nuclei in particular have velocity distributions that are centered on velocities between those of the PLF* and TLF*. In contrast, for nuclei with $3 \leqslant Z \leqslant 15$ (IMFs) the velocity distribution, although broad, clearly has a bimodal nature with each of the two peaks centered close to the PLF* and TLF* velocities. This bimodal character is also observed for helium nuclei although the distributions are broader than for IMFs. These overall patterns manifested for the most peripheral collisions are also observed for more central collisions.

Depicted in Fig. 3 is the dependence of the primary and secondary Z distributions on impact parameter. The Z distribution of particles at $t = 300$ fm/c is the primary distribution and is represented as the solid histogram. Following Coulomb propagation and statistical decay of the excited primary reaction products, the Z distribution of secondary particles is represented by the dashed histogram. The latter distribution includes both primary fragments that did not decay, as well as the decay products of excited primary fragments. All distributions have been normalized to the total number of events for each impact parameter range and therefore represent the average multiplicities. As may be expected from the trends in Fig. 2, the charge distribution for the most peripheral collisions, $b > 10$ fm, is largely dominated by two peaks at $Z = 42$ and 48, which correspond to the TLF* and PLF*. In Fig. 3 we therefore focus on smaller impact parameters, $b \leqslant 10$ fm. In panel (a) the Z distributions integrated over impact parameter up to 10 fm are presented. As expected, the yield for neutrons, hydrogen, and helium is large in the primary distribution (solid histogram). A large yield is also observed for $3 \leqslant Z \leqslant 10$. Evident for $Z \geqslant 30$ is a slight double-peak in the primary distribution attributable to the presence of the PLF* and TLF*. Secondary decay eliminates this double-peak structure as evident in the dashed histogram. To separate the PLF* from the TLF*, as well as to crudely separate their decay products, we further select particles with the condition $V_{\parallel} > 0$. The resulting primary distribution shown in panel (b) manifests only a single peak at large Z, which is located at $Z = 47$. As observed in panel (a) the yield of the Z distribution for $3 \leqslant Z \leqslant 30$ is similar for both the primary and secondary particles.

We examine the dependence of the Z distribution on impact parameter for $V_{\parallel} > 0$ in Figs. 3(c)–3(f). For $8.5 < b \leqslant 10$ fm, Fig. 3(c), the primary Z distribution is V shaped, reminiscent of the U shape observed for asymmetric fission. The minimum yield observed near $Z \approx 20$ is deep in comparison to the yield at lower and higher Z, indicating that asymmetric splits are strongly preferred over symmetric splits. It is striking that the multiplicity for $Z = 3$–6 is approximately the same as that of $Z \approx 47$ (the PLF*). The yield ratio for $Z = 3$–6 over $Z = 45$–47 is $0.31/0.37 \approx 0.84$, indicating a process or processes resulting in copious production of light IMFs. This similarity in the yield of the light IMF and the PLF* can, for example, be understood as the asymmetric binary decay of a precursor PLF*. Such a perspective is supported by experimental observation. For peripheral collisions of two heavy ions at intermediate energies, the phenomenon of dynamical fission is well characterized [45–47]. This dynamical fission has been

associated with the deformation of the PLF* induced by the collision process. The defining characteristics of this process are the aligned asymmetric binary decay of the PLF* and large relative velocities between the two produced fragments. On general grounds one expects that this dynamical process should depend sensitively on both the induced deformation and the excitation of the PLF* [48]. It is important to observe that the shape of this primary distribution largely survives the process of secondary decay. The main difference between the primary and secondary distributions is that the high Z peak is shifted to lower Z and increases in width. For $7 < b \leqslant 8.5$ fm, Fig. 3(d), the shape of the primary distribution is better described as a U shape. In contrast to the previous impact parameter interval, the minimum located at $Z \approx 20$ is shallow. This decrease in the depth of the minimum can be associated with the increase in the probability of symmetric binary splits relative to asymmetric binary splits. This change of the Z distribution with decreasing impact parameter can be related to an increase in the excitation energy of the PLF*. In this impact parameter interval, the yield for $Z = 3$–6 is significantly larger than that for $Z \approx 42$. The ratio of the yield of $Z = 3$–6 over the yield of $Z = 41$–43 is 0.66/0.19 $\approx$ 3.47, a change by a factor of $\approx$4 as the impact parameter decreases from $8.5 < b \leqslant 10$ fm to $7 < b \leqslant 8.5$ fm. This increase in the ratio is because of both an increase in the IMF yield by a factor of 2 and a decrease in the yield in the vicinity of the PLF* peak. The latter decrease reflects the increasing width of the peak in the Z distribution attributable to the PLF* with decreasing impact parameter. Following secondary decay the U shape is somewhat less pronounced. For yet more central collisions, a U-shape distribution is not observed even for the primary distribution. In panel (e) no clear bump is observed at large Z, indicating the decreased likelihood that a high Z PLF* survives to the cluster recognition time of $t = 300$ fm/c. For the most central collisions shown, $b \leqslant 4$ fm, the primary Z distribution is exponential over a large range in Z. This exponential behavior of the yield is suppressed for $Z \geqslant 30$ because of the finite size (atomic number) of the system. The secondary Z distribution for central collisions also exhibits an exponential character for $Z > 3$, although the onset of the finite size effects is observed at $Z = 20$. The main effect of secondary decay on the Z distribution, for all impact parameters, is to significantly enhance the yield of neutrons, hydrogen, and helium nuclei, while decreasing the maximum Z observed, namely the atomic number of the PLF* and TLF*.

IV. VELOCITY DISSIPATION OF THE PLF* AND ITS EXCITATION

The persistence of the binary character of the collision over a large impact parameter range indicates that the PLF* and TLF* might play an important role in understanding the collision dynamics. A quantitative picture of the evolution of the general properties of the PLF* and TLF* with impact parameter is displayed in Fig. 4. For the most peripheral collisions studied, $b > 10$ fm, the $\langle Z_{\mathrm{PLF}^*} \rangle$ is $\approx$48, the atomic number of the projectile. The $\langle Z_{\mathrm{PLF}^*} \rangle$ decreases smoothly with decreasing impact parameter until $b \approx$ 3–4 fm. For

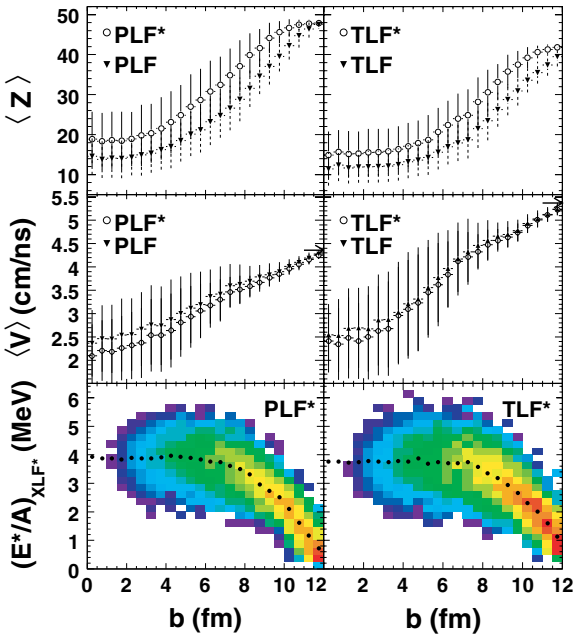

FIG. 4. (Color online) Dependence of the $\langle Z \rangle$, $\langle V \rangle$, and E^*/A of the PLF* and TLF* on impact parameter. Error bars indicate the standard deviation of the distribution. In the bottom panels the solid symbols denote the $\langle (E^*/A)_{\mathrm{XLF}^*} \rangle$ as a function of b.

smaller impact parameters, $\langle Z_{\mathrm{PLF}^*} \rangle$ shows no dependence on impact parameter and has a value of $\approx$19. For $b <$10 fm, $\langle Z_{\mathrm{PLF}} \rangle$, namely the average atomic number following decay, is approximately 4–9 units less than $\langle Z_{\mathrm{PLF}^*} \rangle$ and exhibits the same impact parameter dependence as $\langle Z_{\mathrm{PLF}^*} \rangle$. It should be noted that the largest difference between $\langle Z_{\mathrm{PLF}^*} \rangle$ and $\langle Z_{\mathrm{PLF}} \rangle$ is observed for midperipheral collisions with an impact parameter $\approx$8 fm. The average center-of-mass velocity of the PLF*, $\langle V_{\mathrm{PLF}^*} \rangle$, also exhibits a smooth dependence on impact parameter, decreasing monotonically from $\langle V_{\mathrm{PLF}^*} \rangle \approx$ 4.3 cm/ns for the most peripheral collisions ($V_P = 4.36$ cm/ns) to $\approx$2.5 cm/ns for $b = 3$ fm. For more central collisions $\langle V_{\mathrm{PLF}^*} \rangle$ only shows a weak dependence on impact parameter. With increasing centrality the width of the velocity damping distribution (indicated by the error bars) increases significantly, indicating the growth of fluctuations.

The predicted velocity damping of the PLF* evident in the middle panel is associated with a corresponding increase in the excitation of the PLF* as shown in the bottom panel of Fig. 4. Such an association between velocity damping and excitation has been experimentally observed [49]. Although the average E^*/A of the PLF* rapidly increases with impact parameter for peripheral collisions, it saturates at $\approx$4 MeV by $b = 6$ fm. The trends observed for the PLF* are also observed for the TLF* as depicted in the right column of Fig. 4. It is interesting to note that the $\langle E^*/A \rangle$ for small impact parameters attained for both the PLF* and TLF* is the same despite the smaller size of the TLF* ($Z \approx 15$) as compared to the PLF* ($Z \approx 19$). This difference of $\approx$20–25% in Z corresponds to a similar difference in A (see Fig. 7). Equal partition of E* would thus result in a larger $\langle E^*/A \rangle$ for the TLF* as compared to the PLF*. An $\langle E^*/A \rangle = 4$ MeV

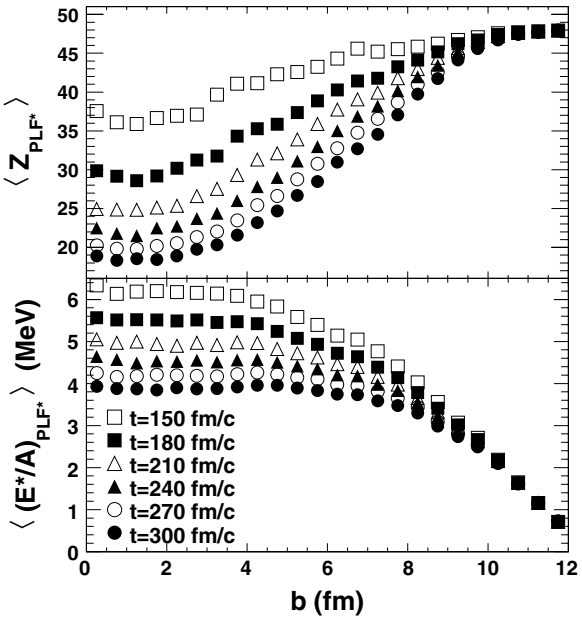

FIG. 5. Dependence of the $\langle Z \rangle$ and $\langle E^*/A \rangle$ of the PLF* on impact parameter for different cluster recognition times.

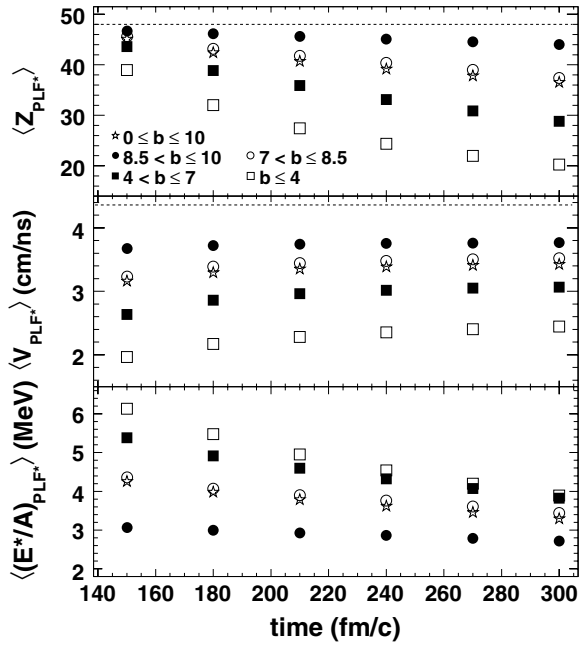

FIG. 6. Dependence of the $\langle Z \rangle$, $\langle V \rangle$, and $\langle E^*/A \rangle$ of the PLF* on cluster recognition time for different impact parameters. The dashed line represents the projectile atomic number (velocity) in the top (middle) panel.

for the PLF* would correspond to an $\langle E^*/A \rangle = 5$ MeV for the TLF*. The similarity of $\langle E^*/A \rangle$ for both the PLF* and TLF* is indicative that the degree to which thermalization is achieved is large or reflects that the $\langle E^*/A \rangle$ has reached a saturation value. For the most peripheral collisions, $b \approx 12$ fm, the nonzero value of the $\langle (E^*/A)_{\mathrm{TLF}^*} \rangle$ and $\langle (E^*/A)_{\mathrm{PLF}^*} \rangle$ is in part because of the mismatch between the binding energy of the projectile and target in AMD and their real binding energies. This error typically ranges from 0.2 to 0.3 MeV. Additional excitation may occur because of the mean-field or Coulomb interaction.

To further characterize the saturation in E^*/A of the PLF* and TLF* for $b < 6$ fm observed in Fig. 4, we have investigated the influence of our choice of cluster recognition time on the atomic number and the excitation energy of the PLF*. We have chosen to recognize the clusters at $t = 150$, 180, 210, 240, 270, and 300 fm/c and compare the dependence of the atomic number and excitation energy on impact parameter for the different cluster recognition times. As evident in the lower panel of Fig. 5, whereas for peripheral collisions the average excitation energy is fairly independent of the choice of cluster recognition time, with decreasing impact parameter the average excitation energy deduced depends significantly on the choice of cluster recognition time. For central collisions, the excitation attained is higher the earlier one recognizes the clusters. For an early cluster recognition time, $t = 150$ fm/c, a maximum value of $\langle E^*/A \rangle \approx 6$ MeV is attained in comparison to $\langle E^*/A \rangle \approx 4$ MeV for $t = 300$ fm/c. For different cluster recognition times one also observes that the onset of the saturation in excitation energy occurs at different impact parameter. For $t = 300$ fm/c the onset of the saturation occurs at $b \approx 6$ fm (≈25% of the cross-section), whereas for $t = 150$ fm/c, the onset occurs at $b \approx 4$ fm (≈10% of the cross-section). The events associated with the highest excitation attainable therefore correspond to a significant fraction of the cross-section. Both the trend and magnitude of $\langle E^*/A \rangle$ is consistent with the AMD calculations for a more asymmetric system [32]. This rapid decrease in $\langle E^*/A \rangle$ is indicative of rapid cooling of the PLF*. This rapid deexcitation of the PLF* results in a rapid decrease of its $\langle Z \rangle$, as shown in the top panel of Fig. 5. For the most central collisions, the size of PLF* decreases by ≈30% between $t = 150$ fm/c and $t = 210$ fm/c. As one may imagine, the choice of a cluster recognition time less than 150 fm/c becomes increasingly problematic because both the conceptual, as well as practical, problem of distinguishing clusters during the high-density phase of the collision.

The dependence of some of the average properties of the PLF* on both impact parameter and cluster recognition time are summarized in Fig. 6. In the top panel, the average atomic number of the PLF*, $\langle Z_{\mathrm{PLF}^*} \rangle$, is displayed as a function of cluster recognition time for different impact parameters. For the most peripheral collisions, $8.5 < b \leqslant 10$ fm, and the shortest cluster recognition times, $\langle Z_{\mathrm{PLF}^*} \rangle \approx 47$, just below $Z_{\mathrm{BEAM}} = 48$ as indicated by the dashed line. Longer cluster recognition times result in a slight decrease in $\langle Z_{\mathrm{PLF}^*} \rangle$ to a value of ≈44 at $t = 300$ fm/c. This reduction in $\langle Z_{\mathrm{PLF}^*} \rangle$ corresponds to the emission of charge on a short time scale. For more central collisions a similar behavior is observed although the magnitude of the charge emitted on a short time scale is considerably larger.

In the middle panel of Fig. 6, the trend of $\langle V_{\mathrm{PLF}^*} \rangle$ with cluster recognition time and impact parameter is presented. For $8.5 < b \leqslant 10$ fm, essentially no change is observed in $\langle V_{\mathrm{PLF}^*} \rangle$ as the cluster recognition time changes from $t = 150$ fm/c to 300 fm/c. For midcentral and central collisions, a small

increase in $\langle V_{\mathrm{PLF}^*}\rangle$ is discernible as the cluster recognition time increases. This slight increase is attributable to the Coulomb reacceleration of the PLF* following the collision combined with recoil effects because of predominantly backward emission of particles on a short time scale.

The dependence of $\langle (E^*/A)_{\mathrm{PLF}^*}\rangle$ on cluster recognition time is depicted in the bottom panel of Fig. 6 for different impact parameters. As previously noted in Fig. 5, for $8.5 < b \leqslant 10$ fm the cluster recognition time has only a weak influence on $\langle (E^*/A)_{\mathrm{PLF}^*}\rangle$. Longer cluster recognition times lead to slightly lower $\langle (E^*/A)_{\mathrm{PLF}^*}\rangle$, 3.1 MeV for $t = 150$ fm/c as compared to 2.8 MeV at 300 fm/c. More central collisions, however, manifest a more marked dependence. As apparent in Fig. 5, for $b < 4$ fm $\langle (E^*/A)_{\mathrm{PLF}^*}\rangle$ reaches a value of 6 MeV for the shortest cluster recognition times, whereas at longer cluster recognition times $\langle (E^*/A)_{\mathrm{PLF}^*}\rangle$ is only ≈4 MeV. This decrease in excitation energy is rapid with most of the decrease occurring from $t = 150$–240 fm/c and is directly related to the emission of particles over this time interval. As the excited PLF* rapidly emits charged particles between $t = 150$–240 fm/c its atomic number decreases, whereas its velocity remains relatively constant. Thus, a proper description of this deexcitation of the highly excited PLF* requires modeling the statistical decay of the early PLF*, which is likely deformed.

The composition of the excited PLF* and TLF* that subsequently undergoes decay is indicated in Fig. 7. In this figure the $\langle N/Z\rangle$ of both the PLF* and TLF* are examined as a function of impact parameter. For $b > 6$ fm, the $\langle N/Z\rangle$ of both PLF* and TLF* evolves essentially linearly with impact parameter from the initial values of 1.375 and 1.19 for the projectile and target respectively. Over this range of impact parameter, this behavior could be interpreted as equilibration of N/Z. However, the change in $\langle N/Z\rangle$ is larger for the PLF* as compared to the TLF* by a factor of 2. This difference reflects the fact that exchange between the PLF* and TLF* is not the only process occurring thus complicating the interpretation of the change in N/Z in terms of equilibration. For more central collisions, the $\langle N/Z\rangle$ remains essentially constant having saturated at a value of ≈1.24–1.26. The similarity of the average N/Z value for the PLF* and TLF* could be interpreted as equilibration of this degree of freedom. If this is indeed the case, it is interesting to note that for $b^* \approx 4$ fm, this equilibration is already essentially achieved. For comparison the $\langle N/Z\rangle$ of the system is ≈1.29. The slightly lower N/Z asymptotic value of the PLF* and TLF* for central collisions as compared to the N/Z of the system suggests either a preferential emission of free neutrons or the production of neutron-rich fragments in the dynamical stage.

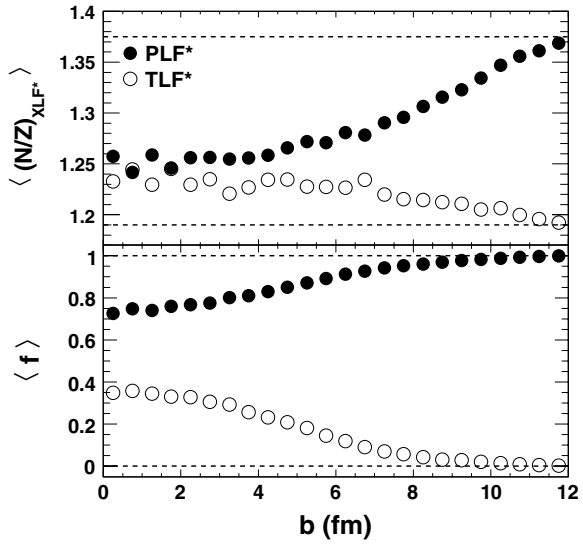

FIG. 7. (Top panel) Dependence of the $\langle N/Z\rangle$ of the PLF* and TLF* on impact parameter. Dashed lines indicate the initial N/Z of projectile and target nuclei. (Bottom panel) Fraction, f, of nucleons found in the PLF* (solid symbols) or TLF* (open symbols) that originate from the projectile.

We examine the degree to which mixing occurs in the lower panel of Fig. 7. In this figure the dependence of f, the fraction of nucleons in the PLF* or TLF* that originate from the projectile, on impact parameter is presented. It is interesting to note that for $b \geqslant 6$ fm, the region in which $\langle N/Z\rangle$ changed linearly with b, the fraction of nucleons in the PLF* that were originally in the projectile is large, $f \geqslant 0.9$. Only for smaller impact parameters does the degree of mixing of projectile and target nucleons become larger. Thus, the large change in $\langle N/Z\rangle$ of the PLF* and TLF* does not require large mixing of the projectile and target nucleons but can be induced by the emission of free nucleons and light clusters. It is instructive to note that the quantity f appears to saturate for $b \leqslant 2$ fm with a maximum of ≈30% of the PLF* nucleons originating from the target. For the TLF*, in the case of small impact parameters, the degree of mixing is similar. It has been experimentally demonstrated that for midperipheral collisions the N/Z degree of freedom does not reach equilibrium [50]. However, the present result indicate that N/Z equilibrium is effectively attained for midcentral collisions, despite the *incomplete mixing* of the projectile and target nucleons. This result is of significance to future work with radioactive beams, indicating the degree to which the N/Z exotic projectile can be excited although only modestly perturbing its N/Z.

Over the past decade considerable attention has been focused on the possible liquid-gas phase transition of nuclear matter induced by either heavy ions [16,51] or multi-GeV hadronic probes [9,10]. A thermodynamic approach to understanding a liquid-gas phase transition requires equilibrium between the gaseous and liquid phases. Within a Fisher's droplet model, clusters (IMFs) can be viewed as manifestations of the nonideal gas [52], whereas the residue (viz. PLF*) can be considered as the liquid phase. Consequently, it is useful to examine how the $\langle E^*/A\rangle$ of IMFs compares to the $\langle E^*/A\rangle$ of the PLF*. To address this question we examine the dependence of $\langle E^*/A\rangle$ on the size of the cluster, A. We have also investigated how this dependence changes with cluster recognition time. Clearly evident in Fig. 8 is the fact that light IMFs, $A \leqslant 40$, and the PLF* (TLF*), $A \geqslant 60$, exhibit a different behavior. In the top panel we present the behavior at early times, $t = 150$ fm/c. Although the $\langle E^*/A\rangle$ for light IMFs increases roughly linearly with A, and is relatively independent of the impact parameter, for $A \geqslant 60$ the $\langle E^*/A\rangle$ depends on impact parameter. For the most

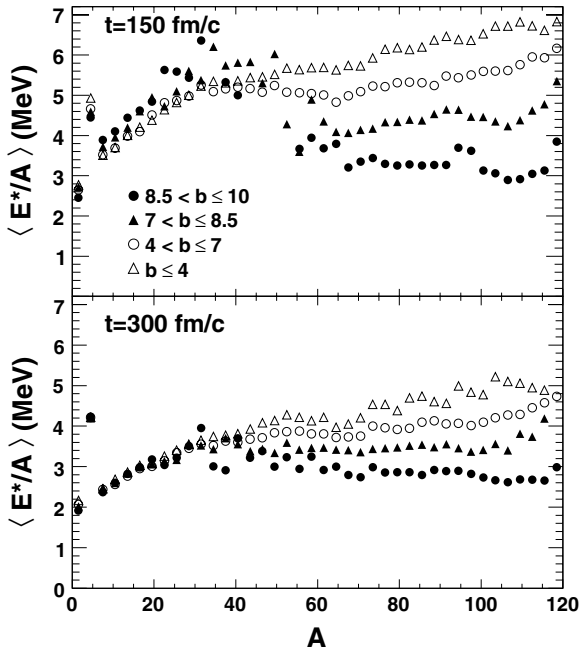

FIG. 8. Dependence of the $\langle E^*/A\rangle$ on A for $t = 150$ fm/c (upper panel) and $t = 300$ fm/c (lower panel).

peripheral collisions presented, 8.5 fm$< b <$10 fm, $\langle E^*/A\rangle$ for the PLF* (TLF*) is essentially independent of size with an average value of ≈3 MeV. With increasing centrality this relative independence of the $\langle E^*/A\rangle$ on the size of the PLF* persists although the magnitude of the $\langle E^*/A\rangle$ increases. For the most central collisions, a slight dependence on A is observed. The same general features manifested at $t =$ 150 fm/c are also evident at $t = 300$ fm/c (lower panel) although the magnitude of the $\langle E^*/A\rangle$ for both the PLF* and IMFs is reduced because of the short time scale emission. These predicted trends do not appear to be consistent with a liquid (PLF*) in thermal equilibrium with its vapor (IMFs).

To summarize the physical picture deduced by examining the properties of the PLF* and TLF*: peripheral and midcentral collisions are largely binary. Both the $\langle Z\rangle$ and $\langle V\rangle$ of the PLF* and TLF* decrease smoothly as centrality increases up to an impact parameter of ≈4 fm. With increasing centrality, the PLF*'s velocity is increasingly damped from the projectile velocity. Concurrent with this damping, the width of the velocity distribution increases. Although the average velocity is largely unchanged by secondary decay, the width of the velocity distribution is typically increased by 10–40%. For smaller impact parameters, $b <$ 3–4 fm, the average atomic number and velocity of the two reaction partners are independent of impact parameter. Associated with these changes in the size and velocity of the PLF* and TLF*, one also observes that the $\langle E^*/A\rangle$ of the PLF* and TLF* increases with decreasing impact parameter from an initial value of 0.7–1.1 MeV up to 4 MeV. The maximum excitation energy is attained for an impact parameter of ≈6 fm. Smaller impact parameters do not result in larger values of $\langle E^*/A\rangle$. These observations suggest that the peripheral collisions on one side and the most central collisions on the other side correspond to different dynamics regime although simulated with the same ingredients.

In peripheral collisions, a transiently deformed PLF* and TLF* are recognizable as early as ≈100 fm/c after the collision. The deformation of these reaction products persists for a considerable time, $t \geqslant 300$ fm/c. In addition to the PLF* and TLF*, nucleons, light charged particles, and IMFs are also produced in the dynamical phase. The latter clusters are preferentially located between the PLF* and TLF*. The Z distribution of particles with $V_{\|} > 0$ strongly favors asymmetric splits. The population of symmetric splits increases for midperipheral collisions reflecting an increase in the excitation energy of the PLF*, which is strongly correlated with the velocity damping. Both the $\langle E^*/A\rangle$ and $\langle V_{\mathrm{PLF}^*}\rangle$ in this impact parameter range are found to be independent of the cluster recognition time. The general insensitivity of $\langle V_{\mathrm{PLF}^*}\rangle$ to cluster recognition time makes it a robust signal of the impact parameter.

In contrast to peripheral collisions, central collisions are no longer dominated by two large fragments, namely the PLF* and TLF*. However, if we designate the largest fragment forward and backward of the center of mass as the PLF* and TLF*, their characteristics, $\langle Z\rangle$, $\langle V\rangle$, and $\langle E^*/A\rangle$, are largely unchanged as b decreases for $b \leqslant 4$ fm. Therefore, for the innermost ≈10% of the total cross-section, the maximum degree of excitation for such collisions is attained. This broad range of impact parameters associated with high excitation underscores the importance of considering the breakup of nonspherical geometries [53]. Moreover, for these small impact parameters, the quantitative characteristics of the PLF* and TLF*, $\langle Z\rangle$ and $\langle E^*/A\rangle$, depend on the cluster recognition time. For early cluster recognition time ($t =$ 150 fm/c) an average excitation energy of 6 MeV is reached, whereas a longer cluster recognition time ($t = 300$ fm/c) results in $\langle E^*/A\rangle$ of 4 MeV. This decrease in $\langle E^*/A\rangle$ indicates a rapid deexcitation during the dynamical stage, also manifested in the decrease of the $\langle Z\rangle$ of the PLF* and TLF*, suggesting significant nucleon and cluster emission on a short time scale.

V. EMITTED PARTICLES

As evident from Fig. 1, as the PLF* and TLF* separate, clusters are produced. This fragment production (as already demonstrated) can occur on a relatively short time scale impacting the Z, velocity, and (E^*/A) of the PLF* and TLF*. To characterize this fast emission process more quantitatively, we examine the multiplicity of fragments produced as a function of impact parameter in Fig. 9. Displayed in Fig. 9(a) is the average multiplicity of fragments, $Z \geqslant 3$, at $t = 300$ fm/c (solid circles). One observes that this multiplicity increases with decreasing impact parameter and saturates for $b \approx 3$ fm. For the most peripheral collisions the average multiplicity is 2, corresponding to the existence of the only PLF* and TLF*. The average fragment multiplicity reaches a value of 3 at $b \approx$ 8–9 fm. For this impact parameter interval, on average, one fragment is produced in coincidence with the PLF* and TLF*. This result is consistent with the asymmetric split of the PLF* deduced from the Z distribution (Fig. 3). As was evident in Fig. 4 this impact parameter also corresponds to the

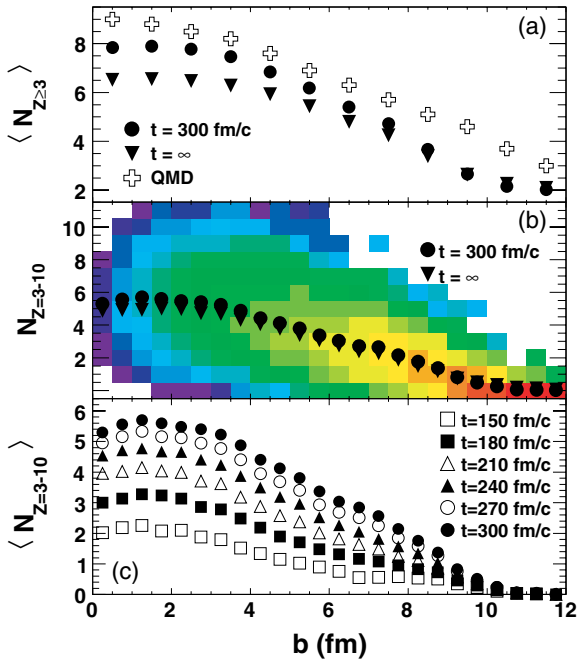

FIG. 9. (Color online) Multiplicity of fragments as a function of impact parameter. (a) Average multiplicity of $Z \geqslant 3$ at $t = 300$ fm/c (solid circles), after secondary decay (solid triangles) and for QMD (open crosses). The QMD results are extracted from Ref. [54]. (b) Multiplicity of $Z = 3$–10. (c) Average multiplicity of $Z = 3$–10 for different cluster recognition times.

maximum difference between $\langle Z_{\mathrm{PLF}^*} \rangle$ and $\langle Z_{\mathrm{PLF}} \rangle$. For the most central collisions, b <3 fm, the average fragments multiplicity is constant and is ≈8. Following secondary decay (solid triangles) the fragment multiplicity is reduced slightly because of the decay of fragments into particles with $Z \leqslant 2$. For b >7 fm the effect of secondary decay on the fragment multiplicity is negligible, whereas for the most central collisions the average multiplicity decreases from 8 to 6.5. The increased excitation energy associated with more central collisions is no doubt responsible for this increased importance of secondary decay. The multiplicities predicted in the present calculation are compared to those from QMD calculations for the system Xe+Sn [54]. Although both systems were simulated for the same incident energy of 50 MeV/nucleon, the Xe+Sn system is ≈20% larger in A and ≈15% larger in Z than the present system. The multiplicity deduced by QMD (open crosses) is larger that the ones of the present work at all impact parameters. Given the difference in the system size, the difference between the multiplicities for $b \leqslant 6$ fm may be reasonable. The most notable feature of this comparison between the two models is the behavior for peripheral collisions, $b \geqslant 8$ fm. In this impact parameter interval, the fragment multiplicities predicted by AMD appear to be more realistic than those predicted by QMD. This difference may be because of spurious decay of the projectile and target in QMD because of the poor description of the ground-state properties in that model.

The multiplicity distribution of IMFs ($3 \leqslant Z \leqslant 10$) as a function of impact parameter is presented in Fig. 9(b) for $t = 300$ fm/c. Although the distribution is narrow for the most peripheral collisions, its width rapidly increases with decreasing impact parameter. The average IMF multiplicity, indicated by the solid circles, evolves from 0 for the most peripheral to ≈6 for $b = 3$ fm. At an impact parameter of ≈9 fm, the average IMF multiplicity reaches a value of ≈1, consistent with Fig. 9(a). The average IMF multiplicity is pretty insensitive to secondary decay as indicated by the triangles. Comparison between the fragment multiplicity, Fig. 9(a), and IMF multiplicity, Fig. 9(b), indicates that on average even for the most central collisions two fragments with a $Z > 10$ are present at $t = 300$ fm/c representing a PLF* and TLF* with approximately 20–25% of the original projectile and target atomic number. This result contradicts the physical picture of a single source often assumed for central collisions.

Displayed in Fig. 9(c) is the average IMF multiplicity dependence on b for different cluster recognition times. The average IMF multiplicity increases with increasing cluster recognition time for all impact parameters. The largest increases are evident for the shortest times, $t \leqslant 240$ fm/c. For all impact parameters, the IMF multiplicity increases by a factor of 2 to 3 between $t = 150$ fm/c and $t = 240$ fm/c. After $t = 240$ fm/c, the IMF production rate is reduced with an increase of 20–40% of the IMF multiplicity between $t = 240$ fm/c and $t = 300$ fm/c.

The average multiplicity of neutrons and light charged particles is examined in Fig. 10 as a function of both impact parameter and cluster recognition time. In the left-hand column of Fig. 10 one observes a monotonic increase of the neutron (open symbols) and proton (closed symbols) average multiplicities with decreasing impact parameter both at

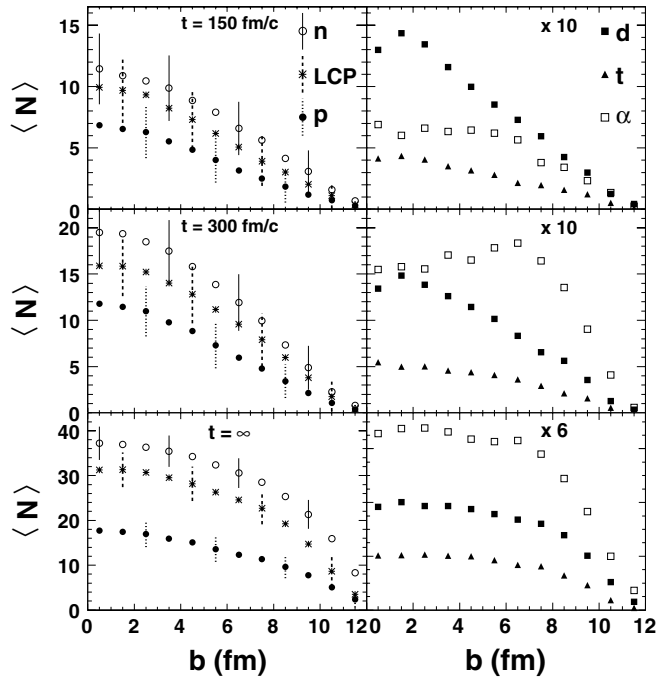

FIG. 10. Multiplicity of neutrons and light charged particles as a function of impact parameter for different cluster recognition times. The multiplicities in the right column have been scaled by the factors indicated. Error bars indicate the standard deviation of the distribution.

$t = 150$ fm/c and $t = 300$ fm/c. At $t = 150$ fm/c a slight saturation in both the neutron and proton multiplicities is observed for the most central collision with maximum average multiplicities of 11.5 and 7 attained. A later cluster recognition time of $t = 300$ fm/c results in approximately a 70% increase in the multiplicities with the saturation of the multiplicities for central collisions being slightly more evident. For this longer cluster recognition time, the average multiplicities associated with central collisions are 19.5 and 12 for neutrons and protons, respectively. Following sequential decay ($t = \infty$), one observes a significant increase in the average multiplicities and a pronounced saturation in the case of the neutrons. This saturation suggests that the total multiplicity (neutron or proton), in particular, although providing impact parameter selectivity for peripheral collisions is a poor selector of more central collisions. Moreover, attempting to select central collisions with the neutron multiplicity would, on the basis of the cross section, be weighted toward midcentral collisions. This result may explain the experimental observation of the persistence of binary collisions associated with large neutron multiplicity [55].

Aside from the difficulty of selecting central collisions by utilizing either the proton or neutron multiplicity, we have also considered which of these measures provides better selectivity for peripheral and midcentral collisions. The larger slope of the neutron multiplicity with impact parameter as compared to the proton multiplicity for $t = \infty$, indicates that neutron multiplicity as compared to proton multiplicity is a better impact parameter selector in this impact parameter interval. When one compares the total neutron multiplicity to the total light charged particle multiplicity (LCP:$Z \leqslant 2$), the difference is considerably smaller. Similar slopes of the multiplicity and fluctuations (error bars) with impact parameter for both neutrons and LCPs indicates that neutrons do not have an inherent advantage as an impact parameter selector except perhaps for the most peripheral collisions. Although the neutron multiplicities are somewhat larger than the LCP multiplicities, consideration of the efficiency for neutron detection mitigates this slight advantage.

In the case of the light cluster (d, t, and α particle) multiplicities (right column of Fig. 10) a couple of points are noteworthy. For short cluster recognition time ($t = 150$ fm/c) the average multiplicity of deuterons is relatively linear over the entire impact parameter range and reaches a value of $\approx$1.4 for the most central-collisions. α particles, in the case of peripheral collisions, manifest similar multiplicities; however, the average multiplicity of α particles saturates for b <6 fm. Tritons exhibit lower multiplicities than both deuterons and α particles for all impact parameters. For longer cluster recognition time, $t = 300$ fm/c, the deuteron and triton multiplicities remain essentially unchanged as compared to $t = 150$ fm/c. In contrast, the α particle multiplicity increases significantly. It is interesting to note that the maximum α multiplicity is not associated with central collisions but rather with $b \approx$ 6–7 fm. From this we conclude that significant α production/emission, but not deuteron or triton emission, occurs on the time scale commensurate with the separation time of the PLF* and TLF* (150 fm/$c \leqslant t \leqslant$ 300 fm/c). Following secondary decay ($t = \infty$) all multiplicities increase significantly. Moreover, only for peripheral collisions, $b \geqslant$ 8 fm, does the average multiplicity of light clusters depend significantly on impact parameter.

We examine the emission pattern for IMFs ($3 \leqslant Z \leqslant 10$) in Fig. 11 both at $t = 300$ fm/c and at $t = \infty$ as a function of impact parameter. In examining the most peripheral collisions for $t = 300$ fm/c, we observe two major components that are shifted with respect to the velocity of the PLF* and TLF* as represented by the arrows in the figure. In addition, a minor component is visible centered at the velocity of the center of mass, i.e., $V_{\parallel} = 0$. This emission pattern is consistent with anisotropic emission in the frame of the PLF* and TLF*. The most likely origin if the observed backward enhancement, i.e., toward midrapidity, is the asymmetry of the collision process itself. With increasing centrality, one observes an increase in

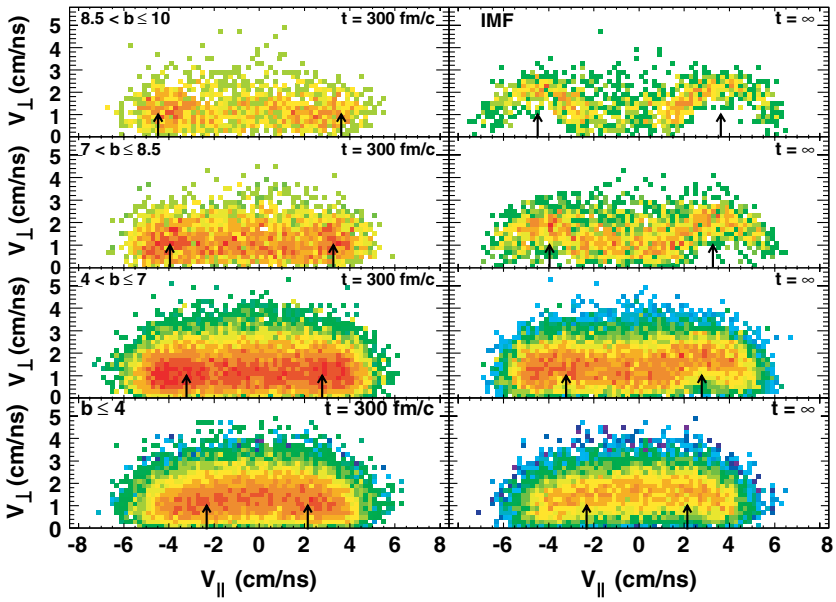

FIG. 11. (Color online) Invariant cross-section for IMFs ($3 \leqslant Z \leqslant 10$) in the COM frame. The arrows indicate the average parallel velocity of the PLF* and TLF*. The color scale indicates the yield on a logarithmic scale. The vertical scale in the bottom two panels has been scaled by a factor of two as compared to the other panels.

this backward yield, as well as an increase in the yield of the midvelocity component. For $b < 7$ fm, this midvelocity yield becomes considerable. For the most central collisions, the distinct bimodal character evident in more peripheral collisions is replaced by a broad distribution. The impact of Coulomb propagation and secondary decay is shown in the right column of Fig. 11. In contrast to the broad distributions observed at $t = 300$ fm/c, the emission pattern following Coulomb propagation to infinite PLF-TLF separation and secondary decay (right column), reveals a pattern of two semicircles centered on the PLF* and TLF* velocities. This pattern is most clearly evident in the case of the most peripheral collisions. Such an emission pattern reflects both the Coulomb focusing in the field of the separating PLF* and TLF*, as well as emission of IMFs from the deexciting PLF* and TLF*. It is important to note that the intensity pattern along each of these Coulomb circles is not constant but exhibits a significant backward enhancement indicating a memory of the initial angular asymmetry. With decreasing impact parameter, the center of these Coulomb circles shifts toward the center of mass and increasingly overlap as the velocity of the PLF* and TLF* decrease. The Coulomb circles also become less distinct with increasing centrality reflecting both increased excitation of the system and nucleon-nucleon scattering.

The parallel velocity distributions of the PLF*, TLF*, and IMFs and their decay products are shown in Fig. 12 as a function of impact parameter. The velocity distributions of the PLF* and TLF* (left column) are presented for reference (shaded histogram). For clarity these latter distributions have been scaled relative to the IMF distributions by the factors indicated. In the case of $8.5 < b \leqslant 10$ fm, the PLF* and TLF* manifest Gaussian-like velocity distributions that are relatively narrow and slightly damped from the beam velocity. With decreasing impact parameter, these two distributions move closer in velocity, i.e., exhibit increased damping, and become broader. The parallel velocity distributions of the PLF and TLF (right column) follow the same general trends as those of the PLF* and TLF*. The widths of the secondary large fragments are typically 10–40 % larger than that of the PLF* and TLF*.

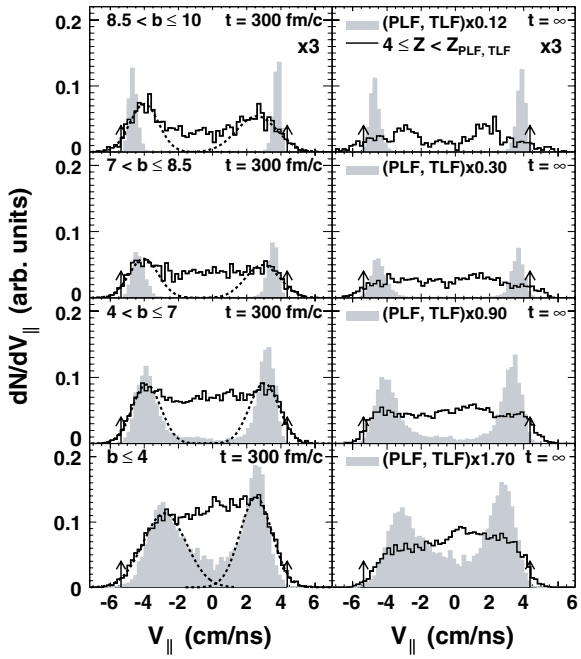

FIG. 12. (Left column) Parallel velocity distributions for the PLF* and TLF* (shaded), as well as IMFs (solid histogram) as a function of impact parameter. The dashed histograms correspond to a two gaussian fit as described in the text. (Right column) Parallel velocity distributions of the PLF, TLF, and IMFs following Coulomb propagation and decay. The IMFs distributions have been normalized to the number of events. The PLF*, TLF*, PLF, and TLF distributions have been scaled relative to the IMFs distributions. The arrows indicate the projectile and target velocities.

For the most peripheral collisions, the IMF velocity distribution (solid histogram) is bimodal with the most probable values of this two peaked distribution displaced toward the center-of-mass velocity as compared to the PLF* and TLF* velocities, clearly establishing the qualitative trend first observed in Fig. 11. In addition to the two Gaussian yields attributable to the emission from the PLF* and TLF* an additional IMF component, smaller in magnitude, is observed. As previously noted in Fig. 11, this additional component has an average velocity roughly centered at the center-of-mass velocity. For $7 < b \leqslant 8.5$ fm, the relative magnitude of the midvelocity contribution is increased. With increasing centrality, the shape of the IMF velocity distribution evolves toward a flat distribution, reflecting increased fragment production at midvelocity.

We have fit the predicted parallel velocity distributions shown with two Gaussians representing the emission from the PLF* and TLF*. The result is depicted as the dashed histogram in Fig. 12. The fit parameters for the PLF* and TLF* emission are presented in Table I. With increasing centrality the centroid of the PLF* velocity distribution decreases and the centroid of the TLF* velocity distribution increases as the reaction is increasingly damped. Although for $b \geqslant 7$ fm a difference between the average parallel velocity for IMFs and the PLF* (or TLF*) is discernible, for $4 < b \leqslant 7$ fm, the IMF distribution is centered on $\langle V_{\mathrm{PLF}^*} \rangle$. The widths of the distributions are presented for completeness. No consistent trend of significance is evident in the extracted widths.

We have also used the two Gaussian fits previously described to extract the average multiplicity associated with the PLF*, TLF* and midvelocity components at $t = 300$ fm/c. The results are tabulated in Table II. With in-

TABLE I. PLF* and TLF* average parallel velocity, and fit parameters for the two Gaussian fit of the IMF $V_\parallel$ distributions at $t = 300$ fm/c. The deduced quantities, $\langle V_\parallel \rangle$ and σ, are expressed in cm/ns.

b (fm)	PLF* $\langle V_\parallel \rangle$	IMF(PLF*)		TLF* $\langle V_\parallel \rangle$	IMF(TLF*)	
		$\langle V_\parallel \rangle$	σ		$\langle V_\parallel \rangle$	σ
$8.5 < b \leqslant 10$	3.76	2.59	1.19	−4.65	−4.01	0.84
$7 < b \leqslant 8.5$	3.51	2.93	1.01	−4.31	−4.03	0.86
$4 < b \leqslant 7$	2.99	3.02	0.87	−3.57	−3.86	0.84
$b \leqslant 4$	2.26	2.55	0.94	−2.48	−2.81	1.25

TABLE II. Average multiplicity of $4 \leqslant Z < Z_{\mathrm{PLF}^*}$, Z_{TLF^*} for the PLF*, TLF*, and midvelocity (MV) components at $t = 300$ fm/c. The relative fraction of the midvelocity component to the total emission is also indicated.

b (fm)	PLF*	TLF*	MV	P(MV)
$8.5 < b \leqslant 10$	0.09	0.09	0.06	0.26
$7 < b \leqslant 8.5$	0.63	0.63	0.81	0.39
$4 < b \leqslant 7$	0.99	0.94	1.53	0.44
$b \leqslant 4$	1.61	1.77	1.51	0.31

creasing centrality the multiplicities for each component increases although for collisions with $b \leqslant 7$ fm the midvelocity multiplicity seems to saturate at a value of $\approx$1.5. From the peripheral collisions, $8.5 < b \leqslant 10$, to the midcentral collisions, $4 < b \leqslant 7$, the average multiplicity of the PLF* and TLF* components increases by a factor $\approx$10 with an increase by $\approx$25 for the midvelocity component. The relative multiplicity of midvelocity emission as compared to the total emission increases from 0.26 for peripheral collisions to 0.44 for more central collisions.

The velocity distributions of the IMFs are significantly altered by secondary decay. This influence is most evident for the peripheral collisions where the shape of the primary distribution is nearly completely destroyed. Naturally, the magnitude of this secondary decay is particularly sensitive to the excitation predicted for the primary fragments. The observed influence of secondary decay on the IMF velocity distribution indicates that the IMFs are significantly excited.

For peripheral collisions, it has been experimentally observed that the emission pattern of α particles emitted by the PLF* manifests an anisotropic distribution [56]. This observed anisotropy has been interpreted as the decay of a PLF* (and TLF*) initially deformed by the collision process. To investigate the extent to which such a physical picture is compatible with the AMD model, we have examined the invariant cross-section maps of α particles. Depicted in Fig. 13 is the dependence of the invariant cross-section map for α particles on impact parameter both at $t = 300$ fm/c and following Coulomb propagation to infinite separation and sequential decay. At $t = 300$ fm/c (left column), for the most peripheral collisions the yield is peaked near the average PLF* and TLF* velocities (indicated by arrows), though slightly toward the center-of-mass velocity. For these most peripheral collisions one observes that the primary α yield centered at midvelocity is relatively small. With decreasing impact parameter, the primary α particle distributions associated with the PLF* and TLF* move closer in velocity and increasingly overlap.

Following secondary decay, the Coulomb circles evident for α particles are even more striking than those for IMFs. This observation is consistent with the large multiplicity of α particles that originate from the deexcitation of the PLF* and TLF* as compared to the early dynamical stage. The distinct emission pattern observed for $8.5 < b \leqslant 10$ fm is also observed for more central collisions although with increasing centrality the distinct nature of the semicircles becomes less striking. The ridge of yield, which is typically interpreted as Coulomb barrier emission, becomes broader and its center moves increasingly toward $V_{\parallel} = 0$. These trends are consistent with the increased damping, excitation, and reduced size of the PLF* (TLF*) with increasing centrality.

Displayed in Fig. 14 is the α-particle yield along the Coulomb ridge for "peripheral" collisions, $5 < b \leqslant 10$ fm, and "central" collisions, $b \leqslant 5$ fm. Alpha particles were selected to be "Coulomb barrier" particles by restriction on their velocities, namely $V_{\alpha} < 3.5$ cm/ns in the PLF* frame. In both cases shown, the total α particle yield (solid histogram) is not symmetric with respect to emission transverse to the PLF* direction, namely $\cos(\theta_{\alpha}) = 0$. Emission in the backward direction, $\cos(\theta_{\alpha}) < 0$, is enhanced with respect to the forward direction. This enhancement is more pronounced for the central collisions. For the peripheral collisions, the emission yield for $\cos(\theta_{\alpha}) = -1$ is approximately 1.7 times the yield emitted in the transverse direction. In contrast, the forward

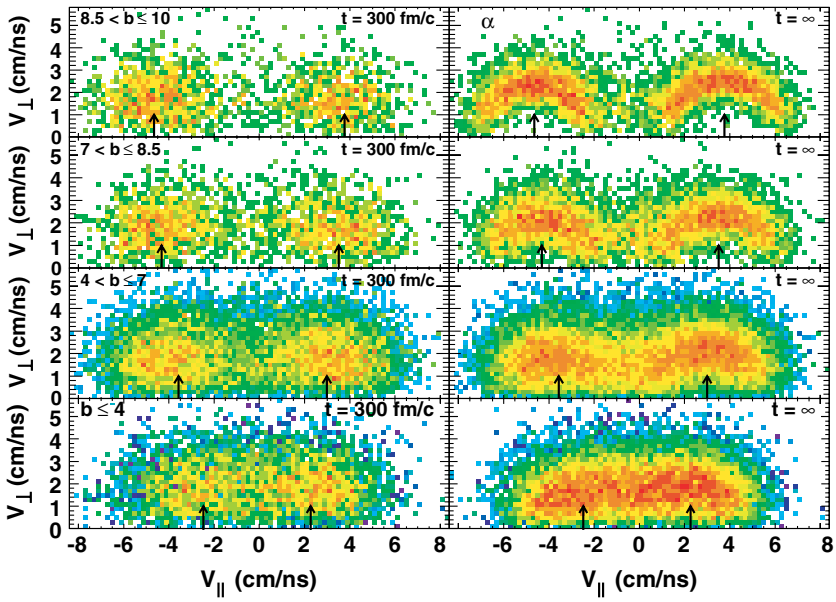

FIG. 13. (Color online) Invariant cross section for α particles in the COM frame. The arrows indicate the average parallel velocity of the PLF* and TLF*. The color scale indicates the yield on a logarithmic scale. In the left column the vertical scale of the bottom panel is scaled by a factor of six as compared to the upper panels. The right column is scaled by a factor of three with respect to the left column.

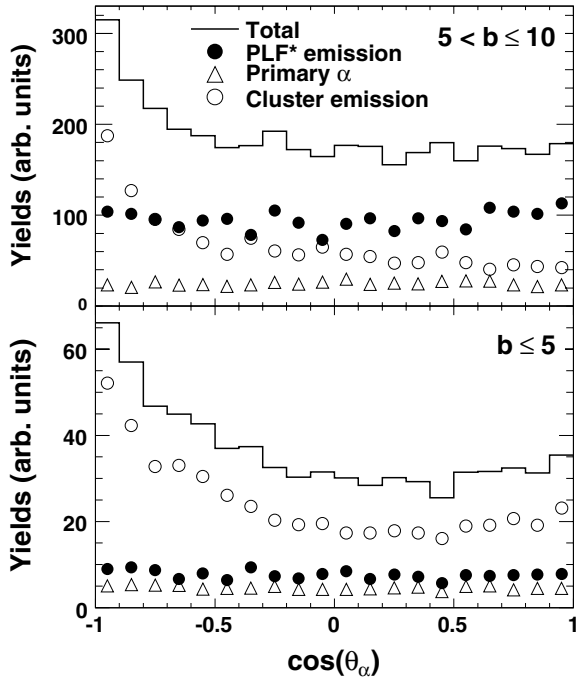

FIG. 14. Angular distribution for α particles on the PLF* Coulomb ridge ($V^*_\alpha < 3.5$ cm/ns). All angles are in the PLF* frame.

emission yield $\cos(\theta_\alpha) = +1$ is approximately the same as the transverse yield. Comparison of the integrated yield with $-1 \leqslant \cos(\theta_\alpha) < 0$, $Y_{\text{backward}}(\alpha)$, to $0 < \cos(\theta_\alpha) \leqslant +1$, $Y_{\text{forward}}(\alpha)$, reveals that backward emission is enhanced by $\approx$19% as compared to forward emission. For more central collisions (bottom panel), comparison of the integrated yield reveals that backward emission is enhanced by $\approx$39% as compared to forward emission.

Within the model calculation, the observed anisotropy has two possible origins: Coulomb focusing of the α particles present at $t = 300$ fm/c and the α decay of IMFs that are emitted anisotropically. We have investigated the origin of this backward enhancement, by examining the possible sources of α particles. α particles are "tagged" as being (a) "primary," namely those originating at the time of cluster recognition ($t = 300$ fm/c), (b) PLF* α particle, or (c) cluster α particle, i.e., those that result from the secondary decay of primary IMFs. As expected, PLF* emission is essentially isotropic. It is evident in Fig. 14 that for both peripheral and central collisions, primary α particles (open triangles) on the PLF* Coulomb ridge are isotropic. Evidently the Coulomb focusing of primary α particles by the PLF* and TLF* does not contribute to the anisotropy observed in Fig. 13. The large backward enhancement observed for the total α-particle yield is associated with the α particles that originate from the secondary decay of primary IMFs. Hence, it is the anisotropy of the primary IMFs that is responsible for the anisotropy of α particles associated with Coulomb barrier energies. Quantitative comparison of the various components reveals that for peripheral collisions the ratio $Y_{\text{backward}}(\alpha)/Y_{\text{forward}}(\alpha)$ associated with the decay of primary clusters is $\approx$2.2, whereas the same ratio for PLF* emission or primary α emission is $\approx$0.9. In the case of more central collisions, the ratio $Y_{\text{backward}}(\alpha)/Y_{\text{forward}}(\alpha)$ associated with the decay of primary clusters is $\approx$1.7. The yield ratio for PLF* emission and primary α emission is $\approx$1.0 in this impact parameter interval.

The anisotropy observed for the decay of primary clusters is consistent with the emission pattern of IMFs as shown in Fig. 11. This feeding of α particles to the PLF* Coulomb ridge from IMF secondary decay is also consistent with the fact that IMFs are produced excited, even for the most peripheral collisions. In fact, the average excitation energy of the IMFs is relatively independent of the impact parameter as shown in Fig. 8. For the most peripheral collisions, $\langle E^*/A \rangle$ of the IMFs is typically 2.5 to 3 MeV with the higher values associated with IMFs produced around the center-of-mass velocity. With increasing centrality, $\langle E^*/A \rangle$ becomes independent of the IMF velocity and reaches a typical value of 3 MeV. Such an excitation energy is in agreement with the excitation energy experimentally deduced for IMFs produced in central collisions [57]. Investigation of the width of the IMF excitation energy distribution reveals that it is large and approximately independent of the impact parameter.

In addition to the anisotropies predicted by the model, in reality the anisotropic emission pattern of α particles can have additional origins. Although the PLF* is clearly deformed for $t \leqslant 300$ fm/c (as shown in Fig. 1), the statistical decay of the PLF* (and TLF*) is assumed to be isotropic. However, if the collision dynamics preferentially "prepares" the system in a configuration that favors emission toward the center of mass, the observed emission pattern will certainly be anisotropic. An example of such a favored configuration would be a dinuclear configuration of the PLF* decaying into an IMF and residue with the IMF preferentially oriented toward midrapidity. If the dinuclear configuration prepared lies outside the saddle point for such a system, then the excitation energy of the dinuclear configuration does not influence the decay probability and the decay is clearly nonstatistical. However, if the dinuclear configuration lies inside the saddle point, excitation energy does influence the decay probability and the emission can be considered statistical. In this case, explicit treatment of the deformation within a statistical framework is necessary [44]. The observed anisotropy under such conditions will depend sensitively on the emission time relative to the rotational period of the dinuclear system. Of course such a schematic description of the binary decay of the PLF* could be extended to ternary and quaternary decays. It should also be noted that such short time-scale emission when the nuclei are in proximity of each other and can also be influenced by tidal effects [43].

The physical picture developed by examining the properties of the PLF* and TLF* is supported by the multiplicities and kinetic characteristics of the emitted particles. The multiplicities of emitted particles increase smoothly with increasing centrality and in some cases saturate. In the case of IMFs, the multiplicity saturates for an impact parameter of $\approx$3 fm. IMF emission is already a likely process for midperipheral collisions with the average IMF multiplicity reaching unity at an impact parameter of $\approx$9 fm by $t = 300$ fm/c. At all impact parameters and for $t > 150$ fm/c, the IMF emission rate decreases monotonically with increasing

cluster recognition time (up to 300 fm/c). Even light charged particles of the same N/Z such as α particles and deuterons exhibit different behavior with respect to cluster recognition time and impact parameter. The α multiplicity, in contrast to that of deuterons, exhibits a large increase between $t = 150$ fm/c and 300 fm/c. Subsequent to secondary decay the multiplicity of light charged clusters (d, t, and α) saturates for mid-central collisions reducing the usefulness of light charged-particle multiplicity as an impact parameter selector. The multiplicity of neutrons also saturates for midcentral collisions, making neutron multiplicity a poor selector of central collisions. Moreover, the geometric cross-section combined together with the saturation of excitation energy for midperipheral collisions may explain the observed persistence of binary collisions at intermediate energies even when the largest neutron multiplicities are selected [55]. In addition to the particle multiplicities, the kinematic properties of the particles provide information about the reaction dynamics. The velocity distribution of the produced IMFs at $t = 300$ fm/c clearly has a bimodal character for peripheral collisions that becomes less distinct as the centrality increases. The IMF velocity distributions reveal preferential emission from the PLF* and TLF* toward the center of mass. The emission pattern of α particles at $t = \infty$ also exhibits a distinct preferential emission toward the center of mass. This anisotropy, however, is not because of the anisotropic emission of primary α particles or evaporation from the PLF* and TLF* but arises from the secondary decay of anisotropically emitted primary IMFs.

VI. CONCLUSIONS

We have examined the dynamical phase of a heavy-ion collision at intermediate energy over a broad range of impact parameter using a microscopic model that includes quantum features, namely the AMD model. Peripheral and midcentral collisions are determined to be largely binary in nature with the excitation of the PLF* and TLF* associated with the velocity damping of the two reaction partners. With decreasing impact parameter the deduced excitation of the PLF*(TLF*) increases; however, it saturates for midcentral collisions. Notably, central collisions do not correspond to higher excitation energy as compared to midcentral collisions as is often assumed. This saturation of the average excitation energy for midcentral collisions implies that the decay of nonspherical geometries is important to consider [53] in understanding the process of fragmentation. The magnitude of the average excitation attained for midcentral collisions is >4 MeV with larger values associated with earlier cluster recognition times. An excitation energy of this magnitude suggests a rapid deexcitation of the PLF*, TLF*, and emitted clusters.

The large excitation energy reached in the collision leads to *rapid particle emission on the dynamical time scale*. This rapid deexcitation underscores that the present two-stage approach of treating the dynamical and statistical decay as decoupled is invalid. The present treatment of the short time-scale decay involves several simplifications. The role of deformation in the decay is neglected as are both Coulomb and nuclear proximity effects. In addition, the excitation energy is calculated relative to clusters that are at the ground state both in shape and density. These simplifications may have a nonnegligible impact on the characteristics of the fragmenting system. Development of a hybrid model that more realistically considers the statistical decay of the transiently deformed nuclei from times as short as 100 fm/c would represent a new and potentially powerful tool in understanding the dynamics of intermediate energy heavy-ion collisions, as well as cluster emission on short time scales.

ACKNOWLEDGMENTS

This work was supported by the U.S. Department of Energy under DE-FG02-92ER40714 (IU) and in part by Shared University Research grants from IBM, Inc., to Indiana University. In addition, A.O. thanks the National Superconducting Cyclotron Laboratory at Michigan State University for the warm hospitality extended to him during his long-term stay.

[1] D. R. Bowman *et al.*, Phys. Rev. Lett. **67**, 1527 (1991).
[2] R. T. deSouza *et al.*, Phys. Lett. **B268**, 6 (1991).
[3] N. Marie *et al.*, Phys. Lett. **B391**, 15 (1997).
[4] M. F. Rivet *et al.*, Phys. Lett. **B430**, 217 (1998).
[5] C. A. Ogilvie *et al.*, Phys. Rev. Lett. **67**, 1214 (1991).
[6] Y. D. Kim *et al.*, Phys. Rev. Lett. **67**, 14 (1991).
[7] E. Cornell *et al.*, Phys. Rev. Lett. **75**, 1475 (1995).
[8] E. W. Cornell *et al.*, Phys. Rev. Lett. **77**, 4508 (1996).
[9] L. Beaulieu *et al.*, Phys. Rev. Lett. **84**, 5971 (2000).
[10] J. B. Elliott *et al.*, Phys. Rev. Lett. **88**, 042701 (2002).
[11] R. P. Scharenberg *et al.*, Phys. Rev. C **64**, 054602 (2001).
[12] N. T. Porile *et al.*, Phys. Rev. C **39**, 1914 (1989).
[13] D. Cussol *et al.*, Nucl. Phys. **A561**, 298 (1993).
[14] D. H. E. Gross, Rep. Prog. Phys. **53**, 605 (1990).
[15] J. P. Bondorf, R. Donangelo, I. N. Mishustin, C. J. Pethick, H. Schulz, and K. Sneppen, Nucl. Phys. **A443**, 321 (1985).
[16] J. Pochodzalla *et al.*, Phys. Rev. Lett. **75**, 1040 (1995).
[17] V. E. Viola, Nucl. Phys. **A734**, 487 (2004).
[18] J. Tõke, J. Lu, and W. U. Schröder, Phys. Rev. C **67**, 034609 (2003).
[19] L. G. Sobotka, R. J. Charity, J. Tõke, and W. U. Schröder, Phys. Rev. Lett. **93**, 132702 (2004).
[20] L. G. Moretto and G. J. Wozniak, Annu. Rev. Nucl. Part. Sci. **43**, 379 (1993).
[21] V. E. Viola, K. Kwiatkowski, J. B. Natowitz, and S. J. Yennello, Phys. Rev. Lett. **93**, 132701 (2004).
[22] R. J. Lenk and V. R. Pandharipande, Phys. Rev. C **34**, 177 (1986).
[23] W. Bauer, Nucl. Phys. **A471**, 604 (1987).
[24] J. Aichelin, Phys. Rep. **202**, 233 (1991).
[25] P. Danielewicz and G. F. Bertsch, Nucl. Phys. **A533**, 712 (1991).
[26] J. Schnack and H. Feldmeier, Phys. Lett. **B409**, 6 (1997).
[27] A. Strachan and C. O. Dorso, Phys. Rev. C **59**, 285 (1999).
[28] K. Morawetz, Phys. Rev. C **62**, 044606 (2000).

[29] A. Chernomoretz, L. Gingras, Y. Larochelle, L. Beaulieu, R. Roy, C. St-Pierre, and C. O. Dorso, Phys. Rev. C **65**, 054613 (2002).
[30] X. Campi, H. Krivine, E. Plagnol, and N. Sator, Phys. Rev. C **67**, 044610 (2003).
[31] D. Cussol, Phys. Rev. C **68**, 014602 (2003).
[32] R. Wada *et al*., Phys. Rev. C **69**, 044610 (2004).
[33] M. Papa, G. Giuliani, and A. Bonasera, J. Comput. Phys. **208**, 403 (2005).
[34] A. Ono, H. Horiuchi, T. Maruyama, and A. Ohnishi, Phys. Rev. Lett. **68**, 2898 (1992).
[35] A. Ono, H. Horiuchi, T. Maruyama, and A. Ohnishi, Prog. Theor. Phys. **87**, 1185 (1992).
[36] A. Ono, S. Hudan, A. Chbihi, and J. D. Frankland, Phys. Rev. C **66**, 014603 (2002).
[37] A. Ono and H. Horiuchi, Prog. Part. Nucl. Phys. **53**, 501 (2004).
[38] J. Dechargé and D. Gogny, Phys. Rev. C **21**, 1568 (1980).
[39] A. Ono and H. Horiuchi, Phys. Rev. C **53**, 2958 (1996).
[40] A. Ono, Phys. Rev. C **59**, 853 (1999).
[41] T. Maruyama, A. Ono, A. Ohnishi, and H. Horiuchi, Prog. Theor. Phys. **87**, 1367 (1992).
[42] F. Pühlhofer, Nucl. Phys. **A280**, 267 (1977).
[43] R. J. Charity *et al*., Phys. Rev. C **63**, 024611 (2001).
[44] R. J. Charity and L. G. Sobotka, Phys. Rev. C **71**, 024310 (2005).
[45] F. Bocage *et al*., Nucl. Phys. **A676**, 391 (2000).
[46] B. Davin *et al*., Phys. Rev. C **65**, 064614 (2002).
[47] J. Colin *et al*., Phys. Rev. C **67**, 064603 (2003).
[48] S. Piantelli, L. Bidini, G. Poggi, M. Bini, G. Casini, P. R. Maurenzig, A. Olmi, G. Pasquali, A. A. Stefanini, and N. Taccetti, Phys. Rev. Lett. **88**, 052701 (2002).
[49] R. Yanez *et al*., Phys. Rev. C **68**, 011602(R) (2003).
[50] M. B. Tsang *et al*., Phys. Rev. Lett. **92**, 062701 (2004).
[51] J. B. Natowitz, R. Wada, K. Hagel, T. Keutgen, M. Murray, A. Makeev, L. Qin, P. Smith, and C. Hamilton, Phys. Rev. C **65**, 034618 (2002).
[52] L. G. Moretto, J. B. Elliott, and L. Phair, Phys. Rev. C **72**, 064605 (2005).
[53] A. le Fèvre, M. Ploszajczak, and V. D. Toneev, Phys. Rev. C **60**, 051602(R) (1999).
[54] R. Nebauer *et al*., Nucl. Phys. **A658**, 67 (1999).
[55] B. Lott *et al*., Phys. Rev. Lett. **68**, 3141 (1992).
[56] S. Hudan *et al*., Phys. Rev. C **70**, 031601(R) (2004).
[57] S. Hudan *et al*., Phys. Rev. C **67**, 064613 (2003).